ISSN 1990-3413, Astrophysical Bulletin, 2025, Vol. 80, No. 3, pp. 502–518. © Pleiades Publishing, Ltd., 2025.
Original Russian Text © The Author(s), 2025, published in Astrofizicheskii Byulleten', 2025, Vol. 80, No. 3, pp. 523–539.

SINIS Detectors in the Subterahertz Range as a Basis for a Receiver for Radio Astronomical Research with the SAO RAS Optical Big Telescope Alt-Azimuth

M. A. Tarasov[1*], A. A. Gunbina[1], A. M. Chekushkin[1], M. A. Markina[1], R. A. Yusupov[1], M. Yu. Fominskii[1], L. V. Filippenko[1], V. S. Edelman[2], V. F. Vdovin[3,4], V. A. Stolyarov[4], I. I. Zinchenko[3], A. M. Krasilnikov[3,4], A. S. Marukhno[3,4], M. A. Mansfeld[3,4], D. E. Kukushkin[4,5], D. A. Sazonenko[4], O. S. Bolshakov[3], A. B. Ermakov[1], I. V. Lesnov[3], and A. F. Valeev[4]**

[1] *Kotelnikov Institute of Radio Engineering and Electronics of the Russian Academy of Sciences, Moscow, 125009 Russia*

[2] *P. L. Kapitza Institute for Physical Problems Russian Academy of Sciences, Moscow, 119334 Russia*

[3] *A. V. Gaponov-Grekhov Institute of Applied Physics of the Russian Academy of Sciences, Nizhnii Novgorod, Russia*

[4] *Special Astrophysical Observatory of the Russian Academy of Sciences, Nizhnii Arkhyz, 369167 Russia*

[5] *ITMO University, St. Petersburg, 197101 Russia*

Received November 26, 2024; revised April 3, 2025; accepted June 6, 2025

Abstract—There is an ongoing need in ground-based astronomy for ultra-sensitive receivers, both coherent (e.g., superheterodyne) and incoherent types, the latter offering potentially higher sensitivity. Both types rely on superconducting or cryogenically cooled semiconductor materials. This study explores the feasibility of using SINIS-based (Superconductor–Insulator–Normal metal–Insulator–Superconductor) detectors as incoherent superconducting receivers. We evaluate the ultimate performance parameters of SINIS detectors depending on the choice of superconducting material, operating temperature, and detection regime. Under moderate sub-Kelvin cooling (down to 0.28 K), aluminum-based SINIS detectors may achieve a responsivity of up to 10^8 V W^{-1} and a noise-equivalent power NEP $= 10^{-17}$ W Hz$^{-1/2}$. For niobium-based SINIS detectors operating at 4.2 K, our estimates yield an NEP $= 1.6 \times 10^{-16}$ W Hz$^{-1/2}$, which may be of practical interest for specific applications. At the Special Astrophysical Observatory of the Russian Academy of Sciences (SAO RAS), a prototype project is underway to develop a domestic subterahertz observatory module integrated with the Big Telescope Alt-azimuthal (BTA). Within this framework, a SINIS-based subterahertz receiver is planned to be installed at the Nasmyth focus of the BTA optical telescope. This paper provides a technical overview and proposed design of the SINIS receiver, taking into account the optical telescope's reflective system architecture, its immediate environment, and the expected scientific goals of such an observational setup.

DOI: 10.1134/S1990341324600996

Keywords: *instrumentation: adaptive optics—submillimeter astronomy—telescopes*

1. INTRODUCTION

At present, research in the field of millimeter and submillimeter-wave astronomy encompasses a wide range of current scientific challenges. Notable examples include investigations of the "cold Universe", star formation processes, and others. The most sensitive detectors employed in such studies are based on superconducting materials and operate at subkelvin temperatures (below 1 K). Depending on the specific objectives, both coherent and incoherent detectors may be used. A major limitation, however, is the absence of specialized subterahertz (sub-THz) telescopes within the territory of Russia. In this context, the potential to utilize a large optical telescope offers numerous new opportunities for advancing observational capabilities in this spectral range. The idea of implementing a superconducting receiver

*E-mail: tarasov@hitech.cplire.ru
**E-mail: aleksandragunbina@mail.ru

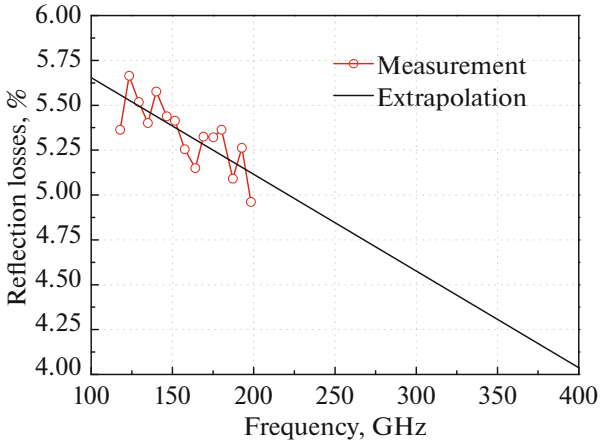

Fig. 1. Reflection losses from the surface of the BTA primary mirror in the sub-THz range: red curve—measurements, black—extrapolation (Fig. 6b from Balega et al., 2024). The study used reference "witness" samples coated in the same deposition cycle as the primary mirror. The coating thickness (about 100 nm) is smaller than the skin depth; in this case, the reflection losses are frequency-independent and amount to several percent.

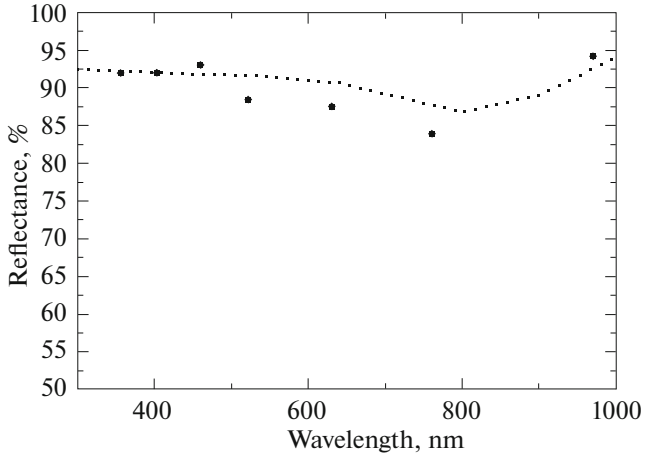

Fig. 2. Reflection coefficient of the BTA primary mirror based on measurements with the CT-7 reflectometer. The dashed line indicates the maximum reflection coefficient for aluminum; dots represent the measured values. For details, see https://www.sao.ru/Doc-k8/Events/2018/MirrorChronicle/.

operating in the sub-terahertz (sub-THz) range on the 6-m BTA telescope at the Special Astrophysical Observatory (SAO RAS) was first introduced in the literature by Vystavkin et al. (2007). However, the initial development efforts began as early as the 1990s but were not brought to completion due to a lack of funding. These efforts were later resumed, with preliminary evaluations presented in the publications by Yakopov et al. (2018) and Balega et al. (2024).

The expected radio astronomical characteristics of the BTA telescope at millimeter wavelengths can be estimated with relative ease. According to Balega et al. (2024), the reflection losses from the BTA's main mirror (hereafter, GM) in this wavelength range are approximately 5% (see Fig. 1).

For comparison, Fig. 2 presents results of the mirror reflectivity measurements in the optical range, based on data available on the official SAO RAS website: https://www.sao.ru/Doc-k8/Events/2018/MirrorChronicle/. The optical mirror of the telescope possesses an almost ideal surface quality for the sub-THz wavelength range. Its geometrical collecting area is approximately 28 m^2. Taking into account reflection losses and mirror obscuration, one can expect a surface utilization factor (SUF) of about 0.7 under a "standard" Gaussian illumination profile, truncated at the mirror edge at the −12 dB level (Baars, 2007). This yields an effective area of approximately 19 m^2. The main beam efficiency under these conditions is estimated to be close to 0.8. The half-power beamwidth (HPBW) will be approximately $HPBW \approx 1.2\,\lambda/D(\text{radians}) \approx 2'$, at a wavelength of 3 mm. This corresponds to a linear resolution of 0.6 pc at a distance of 1 kpc. When transitioning to shorter wavelengths, such as $\lambda = 1.3$ mm or even 0.8 mm, characteristic of instruments like the Event Horizon Telescope[1)], the main beam width and corresponding linear resolution decrease by a factor of two to four. At these wavelengths, the beamwidth may reach approximately 30′, yielding a linear resolution of 0.15 pc at a distance of 1 kpc. However, the geographical location of the BTA telescope is not optimal for observations at these wavelengths. At 1.3 mm, and especially at 0.8 mm, atmospheric absorption (with an optical depth exceeding 0.1 Np) imposes significant constraints on the available observing time. For $\lambda = 1.3$ mm, only several dozen clear days per year are suitable, while for 0.8 mm, the number of feasible observation days is likely limited to fewer than ten.

To assess the potential sensitivity of the BTA in radio astronomy applications, it is instructive to first consider an idealized scenario in which system noise is dominated exclusively by atmospheric emission, and receiver noise can be neglected.

Assuming a zenith atmospheric optical depth of 0.1—which approximately corresponds to typical absorption conditions at the BTA site during "good"

[1)]https://www.cfa.harvard.edu/facilities-technology/telescopes-instruments/event-horizon-telescope-eht

observing seasons (Balega et al., 2024)—the resulting sky brightness temperature at a mean zenith angle of 45° is estimated to be about 35 K. For a receiver bandwidth of 10 GHz operating in modulation mode, the thermal sensitivity achieves approximately 0.7 mK with an integration time of 1 s. The corresponding noise-equivalent flux density (NEFD) is estimated at NEFD $\sim$ 100 mJy Hz$^{-1/2}$.

It is important to note that in real observational conditions, the achievable sensitivity will degrade due to fluctuations in atmospheric absorption and, consequently, in sky emission—even under clear-sky conditions. For instance, a minor variation in atmospheric optical depth by only 0.001 can lead to a change in sky brightness temperature of approximately 0.3 K, which is orders of magnitude greater than the calculated sensitivity limit. To suppress the impact of atmospheric fluctuations, it is essential to employ specialized signal acquisition techniques, such as beam switching or pattern modulation.

2. TYPES AND CHARACTERISTICS OF INCOHERENT DETECTORS IN THE MILLIMETER-WAVE RANGE

Based on their detection mechanisms, microwave detectors and bolometers can be broadly categorized into two major types: thermal detectors and photon detectors. In thermal detectors, the incoming radiation power is uniformly distributed across the volume of the sensing element, resulting in a temperature rise. In photon detectors, the absorption of individual photons induces a current flow through the detector. These two categories can also be further classified by the material used—most commonly: semiconductors, superconductors, and normal metals. A recent comprehensive review of bolometers is given by Zhou and Yeow (2024). Table 1 summarizes the typical characteristics of the most widely used millimeter-wave detectors, including: the Golay cell (optical-acoustic transducer, OAT), pyroelectric detectors, Schottky diodes, SINIS structures (Superconductor–Insulator–Normal metal–Insulator–Superconductor), TES (Transition–Edge Sensors), KID detectors (Kinetic Inductance Detectors), including MKID (Microwave KID) and TKID (Thermal KID), SIS detectors (Superconductor–Insulator–Superconductor, also known as STJ—Superconducting Tunnel Junction), MDMDM structures (Metal–Dielectric–Metal–Dielectric–Metal), HTS STJ (High-Temperature Superconducting Tunnel Junction), HEB (Hot Electron Bolometers), RFTES (Radio Frequency Transition Edge Sensors) and graphene-based detectors. Typical characteristics for some uncooled detectors can also be found in Rogalski (2022).

3. MICROSTRUCTURE OF A SINIS DETECTOR

A schematic representation of a single-detector SINIS structure is shown in Fig. 3. The sensitive element of this type of detector is a nanoabsorber (or absorber) fabricated from a normal metal, which is heated by incoming radiation.

Depending on the operating conditions, a SINIS detector can function based on either a bolometric response mechanism or a photon-counting regime (Devyatov et al., 2006).

In the photon-counting mode, the current response can approach the theoretical limit corresponding to the tunneling of a single electron per absorbed photon. In the quantum bolometer regime, energy multiplexing becomes possible: the number of tunneled electrons approaches the ratio of the photon energy hf to the thermal energy kT. Regarding spectral characteristics, SINIS detectors do not exhibit a fundamental upper frequency limit.

The parameters of SINIS detectors under various operational modes are summarized in Table 2.

4. FABRICATION TECHNOLOGY OF SINIS DETECTORS

Traditionally, SINIS detectors have been fabricated using the shadow evaporation technique of aluminum films. In this approach, the normal metal component was also aluminum, but with a sublayer of iron approximately 2 nm thick, which served to suppress the superconducting properties of the aluminum film.

A modified method for fabricating SINIS structures with an absorber deposited on a substrate involved the so-called "Manhattan" technology, wherein deposition was carried out into orthogonally aligned narrow grooves in the resist. This technique eliminated the need for fragile resist bridges and enabled the fabrication of tunnel junctions with varying areas (we tested junction sizes ranging from 0.1×0.1 to 1×1 μm).

Subsequent advancements in technology have been aimed at moving away from shadow evaporation, focusing instead on the development of SINIS structures with a suspended absorber—i.e., a normal-metal absorber physically separated from the substrate.

At present, the fabrication of SINIS structures is based on a split-lithography process combined with magnetron sputtering (Tarasov et al., 2021a). The core concept of this method involves the separate formation of the superconducting electrodes and the tunnel barrier with the normal-metal absorber. To ensure high-quality tunnel junctions, the surface of the

Table 1. Main types of incoherent detectors for the millimeter-wave range and their typical characteristics

Type*	Responsivity	NEP, W $Hz^{-1/2}$	Frequency modulation	Temperature, K	References
Golay cell (OAP)					[1]
Tydex GC-1P**	10^5 V W^{-1}	10^{-10}	20	300	
Pyroelectric (MG32)	6×10^3 V W^{-1}	10^{-9}	250	300	
	2.6×10^5 V W^{-1}	6×10^{-9}	20	300	[2]
		2×10^{-7}	20	300	[3]
	10^7 V W^{-1}	6×10^{-10}	23	300	[4]
Schottky	6×10^3 V W^{-1}	10^{-12}	1000	300	
		300×10^{-12}		300	[5]
	500×10^3 V W^{-1}	10×10^{-12}		300	[6]
MDMMDM	40 A W^{-1}	10^{-12}	1000	300	
	2.9×10^3 A W^{-1}	1.6×10^{-17}		4.2	[7]
SINIS					
	2×10^8 V W^{-1}	10^{-17}	1000	0.3	[8]
		1.6×10^{-17}		0.27	[9]
TES					
		1.23×10^{-17}	10	0.1	[10]
		7×10^{-17}	0.1÷20	0.51	[11]
		4.7×10^{-17}		∼0.48	[12]
KID					
TKID		2×10^{-17}		∼0.4	[13]
MKID		5×10^{-18}	∼1000	∼0.1	[14]
KID		2×10^{-19}		∼0.12	[15]
SIS (STJ)	2×10^3 A W^{-1}	10^{-16}	10^9	4.2	
	10^9 V W^{-1}	1.6×10^{-16}		≤0.8	[16, 17]
HTS STJ	7×10^3 V W^{-1}	$10^{-11} \div 10^{-13}$(50 K)		60	[18]
HEB		3×10^{-18}	∼700	0.05	[19]
RFTES		3×10^{-17}		0.4	[20]
Graphene	7×10^4 V W^{-1}	3×10^{-13}		25	[21]

* Full detector type names are provided in the main text (see Section 2);

** https://www.tydexoptics.com/ru/products/thz_devices/golay_cell/. [1]—Golay (1947), [2]—Minin et al. (2021), [3]—Müller et al. (2015), [4]—Paulish et al. (2020), [5]—Prikhodko et al. (2021), [6]—Yadav et al. (2023), [7]—Tarasov et al. (2021b), [8]—Tarasov et al. (2022), [9]—Schmidt et al. (2005), [10]—Nunez et al. (2022), [11]—Sayre et al. (2012), [12]—Henning et al. (2012), [13]—Chai et al. (2024), [14]—Yates et al. (2011), [15]—Bueno et al. (2018), [16]—Ariyoshi et al. (2009), [17]—Ariyoshi et al. (2012), [18]—Du et al. (2015), [19]—Karasik and Cantor (2011), [20]—Merenkov et al. (2022), [21]—Generalov et al. (2024).

superconducting aluminum electrodes is pretreated in the deposition chamber using ion etching, followed by controlled oxidation to form a thin insulating layer. A schematic representation of the SINIS fabrication process is presented in Tarasov et al. (2021a). The process begins with the deposition of a bilayer re-

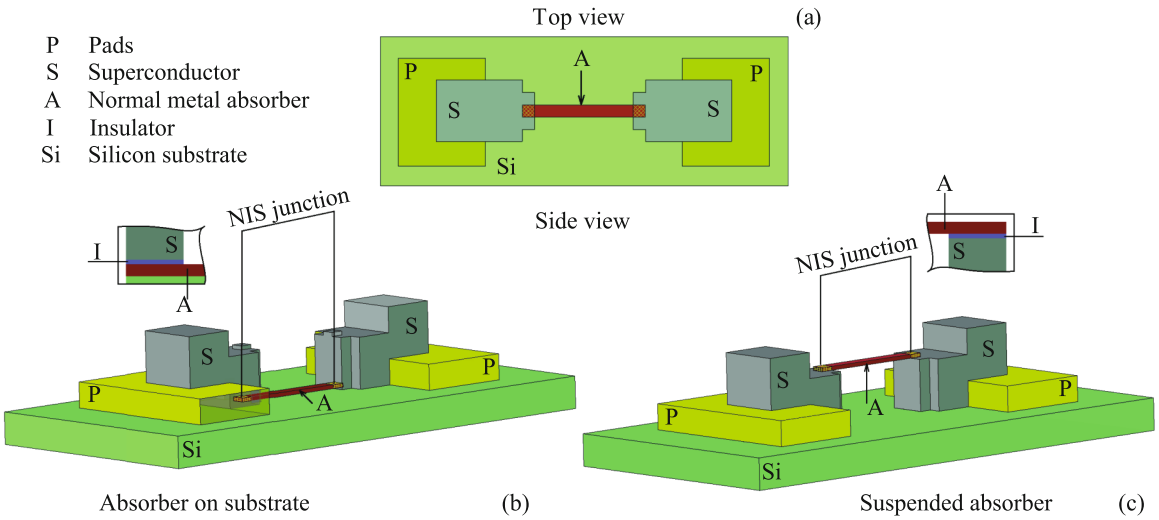

Fig. 3. Schematic representation of various SINIS detector designs: top view (a), side view of a structure with an absorber on a substrate (b), and with a suspended absorber (c).

Table 2. Ultimate parameters of a SINIS detector: bolometric and quantum response modes

Detector mode	Current responsivity	dI/dP, A W^{-1}	dV/dP, V W^{-1}
Photon counter with electron cooling	e/hf	762	2.6×10^7
Real detector biased at half the gap R_d	$2/V_\delta$	5×10^3	1.75×10^8
Quantum detector near the gap $R_d = 2$ kΩ	$e/2kT$	2.2×10^4	4.4×10^7
Electrical bolometer in DC mode	$2k/(R_d e \Sigma \nu T^4)$	3.7×10^5	1.3×10^{10}

sist onto a cleaned silicon substrate (Si) containing predefined contact electrodes (P) (see Fig. 4a). The bottom copolymer layer is essential for creating an undercut profile, which ensures that the deposited metal film remains intact during lift-off and does not peel away with the resist. Following this step, a thin aluminum film is deposited to form the superconducting electrodes. Through the open windows in the resist mask, the film is selectively deposited onto the exposed areas of the substrate (Fig. 4b). After the removal of the initial resist mask (Fig. 4c), a second bilayer resist is applied to the substrate (Fig. 4d) in preparation for the formation of the insulating barrier and the normal-metal absorber. Prior to absorber deposition, the surface of the superconducting electrodes is pre-cleaned in the sputtering chamber by means of plasma etching to remove any parasitic oxides that may have formed. The insulating layer (I) is formed by controlled oxidation of the aluminum electrodes through oxygen exposure in the chamber. Following this step, the absorber layer consisting of a normal metal (N) is deposited (Fig. 4e). A schematic of the completed SINIS structure after lift-off of the second resist layer is shown in Fig. 4f.

5. READOUT ELECTRONICS

One of the key components of receiver systems is the readout electronics, which, like all other elements of the detection system, contributes intrinsic noise.

In the context of ground-based observations, conventional warm readout electronics traditionally employed with SINIS detectors generally meet performance requirements. However, for more sensitive applications such as balloon-borne or, especially, space-based observatories, or for large-format multipixel arrays, it becomes essential to reduce the noise level of the readout system. This can be achieved, for instance, by adopting readout architectures based on high-Q coplanar resonators coupled with cryogenic low-noise amplifiers.

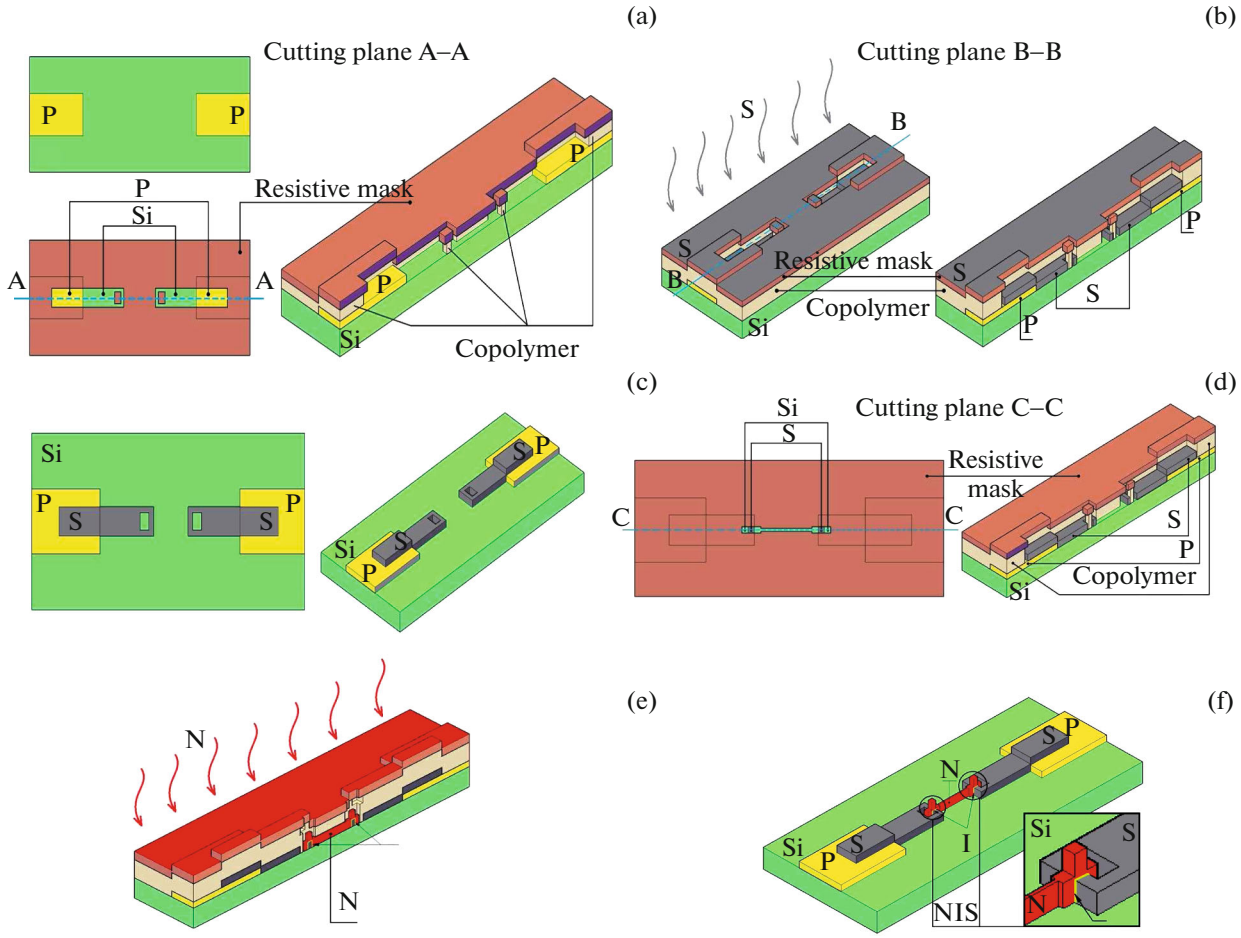

Fig. 4. Fabrication sequence of a SINIS structure using a split lithography process and magnetron sputtering. The following layer designations are used: Si—silicon substrate; P—PADS layer comprising planar antenna elements, interconnects, and bonding pads; S—superconducting electrodes (aluminum); I—tunnel barrier formed by oxidized aluminum; N—normal metal (palladium). For details on stages (a)–(f) see the main text.

This section discusses both configurations: the "classical" warm electronics based on JFET[2)], typically used with SINIS detectors and a microwave readout scheme utilizing niobium coplanar resonators and cryogenic HEMT[3)] amplifiers.

5.1. Uncooled Readout Electronics

The warm readout electronics for SINIS detectors is typically implemented using operational amplifiers based on JFET or MOSFET[4)] transistors operating at room temperature. In general terms, the system operates as follows (a schematic is shown in Fig. 5): a constant bias current is applied to the sample, and the voltage drop across the device is measured. A four-wire configuration is used to eliminate the influence of wiring resistance.

Laboratory measurements and data acquisition are performed using specialized ADC–DAC boards manufactured by National Instruments (USA), which are also planned for use in the initial tests of the receiver on the BTA telescope. These boards are controlled via a personal computer running custom software, `IRTECON`, developed by Ermakov et al. (2001). The biasing circuit employs a symmetric configuration using two 820 kΩ resistors located on a connector within the "cold" part of the cryostat, connected in series with the SINIS structure. The measured noise level of this system is approximately 20 nV/Hz$^{1/2}$. In parallel with the test version, an alternative readout system is being developed based on a microcomputer and a domestic external ADC/DAC module, the LCARD E14-140M-D-m. Another option under consideration is a readout scheme utilizing the ELBEAR ACE-UNO board, built around the MIK32 AMUR (K1948VK018) microcontroller—the

[2)] Junction field effect transistor.
[3)] High Electron Mobility Transistor.
[4)] Metal-Oxide-Semiconductor Field-Effect Transistor.

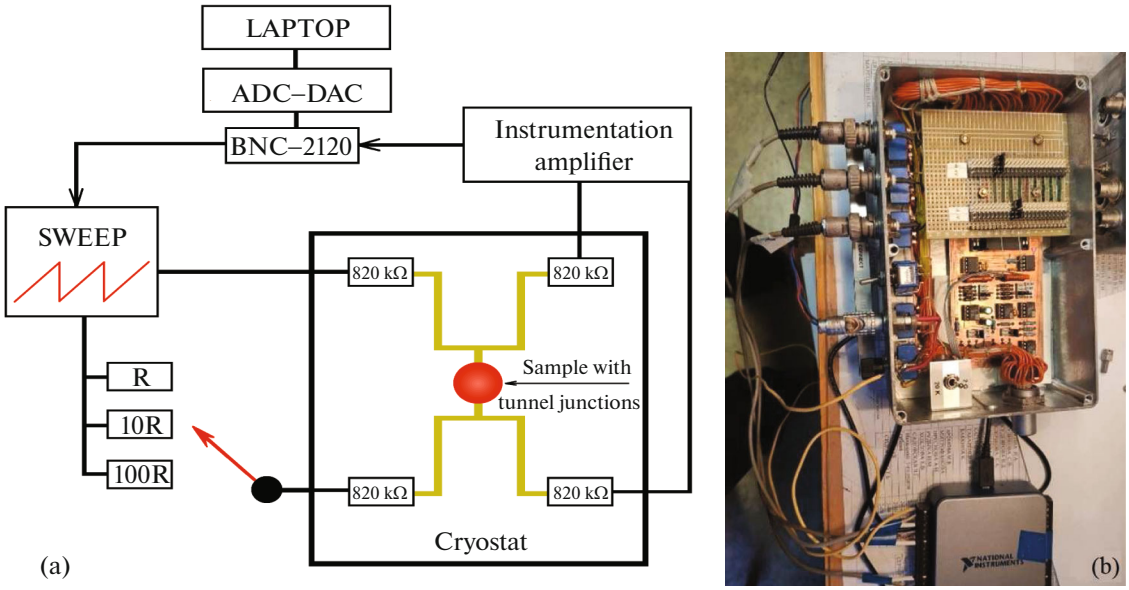

Fig. 5. Readout electronics based on non-cryogenic amplifiers: schematic representation of the measurement principle (a); photograph of the readout module utilizing low-noise instrumentation amplifiers (b).

first fully domestic processor with a RISC-V[5] open-architecture core.

The data acquisition system under development will not only provide readout of the SINIS detector signals and control of the cryogenic system that cools the detectors, but will also support logging and monitoring of the telescope's guidance system, tracking modes of observed objects, and modulation diagram control. The system will be closely integrated with the telescope's main control infrastructure. The data exchange protocol with the remote microcomputer is based on the gRPC[6] framework, which offers bidirectional streaming, flow control, blocking and non-blocking bindings, as well as support for cancellation and timeout mechanisms. In addition, the system supports a wide range of programming languages, providing flexibility in the development of client applications for data acquisition and processing.

Another promising avenue for the development of advanced SINIS detector readout systems is the use of FPGAs[7]. This solution is primarily oriented toward future large-scale detector arrays, where rapid, real-time data processing is essential. Owing to their high-speed parallel computing capabilities, FPGAs are widely regarded as the most efficient architecture for intensive signal processing tasks, including those found in machine vision and astronomical imaging.

Observations conducted with modern telescopes generate large volumes of data that must be processed in real time. FPGAs are ideally suited for such workloads, as they enable low-latency operations such as signal filtering, data correlation, and adaptive optics control. These features are especially critical for detecting and tracking fast transient events, such as supernova bursts or cosmic ray interactions.

One of the key advantages of FPGA technology lies in its flexibility and configurability for specific tasks. In the context of astronomical telescopes, this implies that the processing architecture can be readily adapted to evolving scientific objectives, modifications in data processing algorithms, or the integration of new types of sensors.

For instance, an FPGA-based system can be reconfigured to perform spectral analysis, real-time correlation of radio signals, or on-the-fly image processing. Such adaptability makes FPGAs particularly well-suited for next-generation observatories, where the capability to tailor signal processing pipelines to specific observational programs is essential.

As an additional readout system option for this project, the Xilinx Kria KR260 Robotics Starter Kit was selected. This platform is essentially a microcomputer based on ARM architecture processors[8] combined with FPGA, within a System on Module (SoM), specifically the Zynq UltraScale + MPSoC EV (XCK26). Compared to widely used

[5] Reduced Instruction Set Computer.
[6] Remote Procedure Call.
[7] Field-Programmable Gate Array.
[8] Advanced RISC Machine.

single-board computers such as the Raspberry Pi, the main advantage of such systems is the ability to implement custom logic components (e.g., Fourier processors, correlators, FIR/IIR[9]), using FPGA resources. These components operate in real time and share data with the processor cores via a common data bus, while service functions such as FPGA control, Ethernet interface management, and others are handled by the onboard operating system (e.g., FreeRTOS or Linux).

The Kria KR260 platform is considered for future use when the need arises for multi-channel ADC readout and real-time signal processing (e.g., compression, filtering). The working version of the readout electronics, based on domestic hardware, will be integrated into the hardware-software control system of the BTA telescope. In order to enable coordinated measurements, integration with experimental setup control software supporting SCADA[10] (e.g., EPICS[11] is also under consideration.)

5.2. Microwave Readout System

An alternative to the non-cryogenic readout electronics is a cryogenic microwave readout system based on high-Q superconducting coplanar resonators located inside the cryostat in close proximity to the detectors (see Fig. 6). This configuration offers several key advantages:

- a single coaxial cable can be used to read signals from multiple detector elements or arrays. In contrast, traditional warm readout electronics would require a large number of individual signal and bias lines, each of which contributes additional thermal and electronic noise;
- the use of cryogenically cooled amplifiers, such as high electron mobility transistors (HEMTs) or Josephson traveling-wave parametric amplifiers, significantly reduces the intrinsic noise of the system;
- operating in the microwave frequency range allows for a substantial decrease in flicker noise compared to JFET-based readout schemes that rely on DC biasing;
- a more compact system design.

A high-quality-factor resonator is implemented as a coplanar quarter-wavelength transmission line made of a superconducting material. The detector or detector array is connected as a load at one end of the resonator. The opposite end is capacitively coupled to

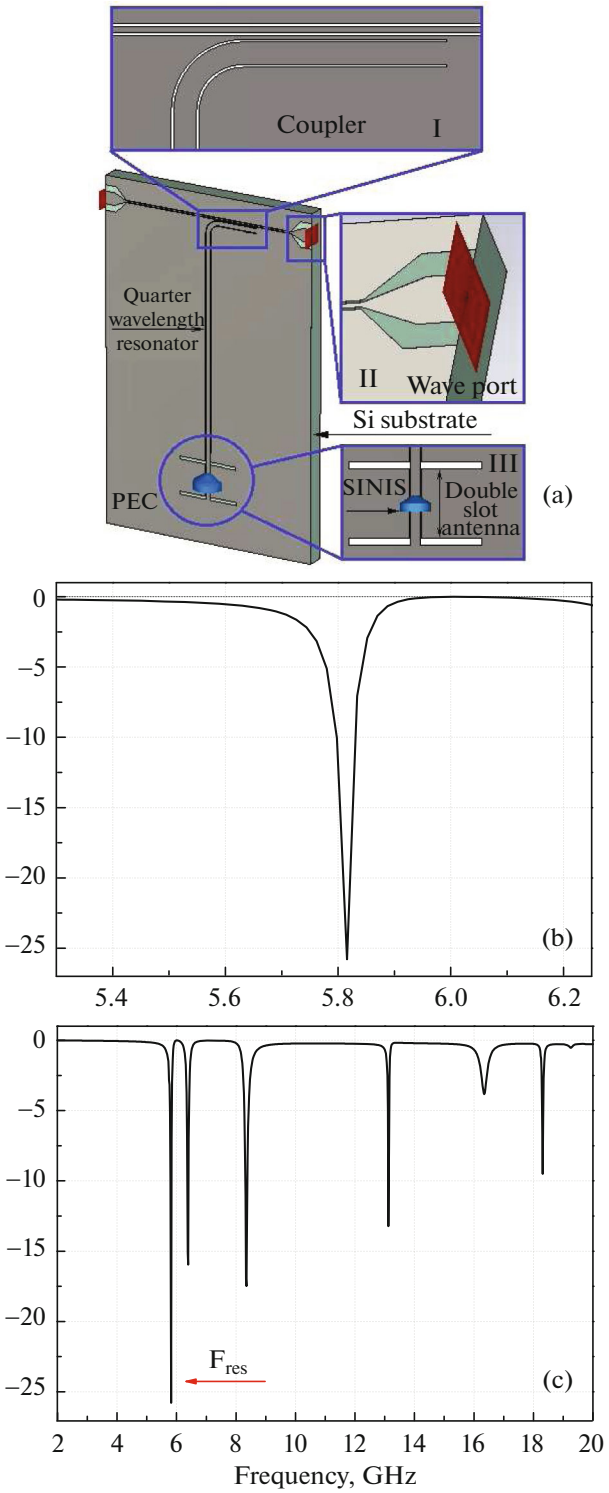

Fig. 6. Schematic representation of the elements of a microwave readout system for SINIS detectors: simulated structure tuned to a resonance frequency of F_{res} 6 GHz (a), I—coupling node (coupler), II—wave port, III—PEC (perfect electric conductor); S21-parameter of the structure in a narrow frequency range (b); S21-parameter of the structure over a broad frequency range (c).

[9] Finite Impulse Response (FIR) and Infinite Impulse Response (IIR) filters.
[10] Supervisory Control And Data Acquisition.
[11] Experimental Physics and Industrial Control System.

a feedline. Multiple such resonators, each tuned to a different frequency, can be connected to a single feedline, enabling multiplexed readout. Initial research on the integration of this readout approach with SINIS detectors was presented in Tarasov et al. (2020b) and Gunbina et al. (2021a). The cryostat system was upgraded to incorporate a cryogenic (thermally insulated) coaxial line, and a custom sample holder was developed. The experimental setup and the measured resonance response are shown in Fig. 7.

6. STRUCTURES BASED ON Nb–AlO_x–Al

The parameters of Al–AlO_x–Pd–AlO_x–Al structures at temperatures of 300 mK and below are often excessive in terms of responsivity and noise-equivalent power (NEP) under realistic ground-based observing conditions (i.e., observations through the atmosphere using a telescope). In such cases, SINIS-type structures based on Nb–AlO_x–Pd–AlO_x–Nb, operating at liquid helium temperatures, can be employed. Figure 8 shows the differential resistance of Nb-based SIN chains consisting of 2, 10, 20, and 50 junctions measured at 2.8 K, which is the temperature achievable by the second stage of a closed-cycle Gifford-McMahon (GM) cryocooler (Markina et al., 2024). For these detectors, both GM cryostats and pulse-tube (PT) cryocoolers are suitable.

Using a closed-cycle cryocooler ensures uninterrupted detector operation without requiring liquid helium or nitrogen. However, when operating on the BTA telescope, it may be advantageous to minimize vibrations and electromagnetic interference from the cryocooler compressor. To address this, a helium recondensation regime can be implemented: during daytime, when the BTA telescope is unavailable for optical observations, gaseous helium from a storage tank is recondensed; during nighttime observations, the compressor is switched off to enable highly sensitive measurements. This mode—maintaining cryogenic temperatures for up to eight hours—was successfully demonstrated in the work of Edelman and Yakopov (2013).

The current responsivity slope changes significantly when switching from superconducting aluminum to superconducting niobium, decreasing by a factor of $1400/140 = 10$, from 5×10^3 to 5×10^2 A W^{-1}. For comparison, the responsivity of MIMIM structures (metal–insulator–metal–insulator–metal) varies from 4×10^4 at 0.28 K to 2.9×10^3 at 4 K. An advanced approach to detector design involves MIMIM-type structures in which the central metal acts as a suspended microwave absorber above the substrate. These structures show enhanced responsivity and are a promising direction for further development of high-sensitivity detectors. The current responsivity of the MIMIM structures considered below ranges from 4×10^4 at 0.28 K to 2.9×10^3 at 4 K.

Table 3. Estimated ultimate parameters for MIMIM quantum detectors at different operating temperatures (Tarasov et al., 2020a)

T, K	S, A W^{-1}	NEP, W $Hz^{-1/2}$
0.28	4.3×10^4	2.8×10^{-17}
4.2	2.9×10^3	1.6×10^{-16}
77	160	1.25×10^{-15}
300	40	10^{-14}

7. MIMIM DETECTORS

The operating principle of MIMIM detectors differs little from that of the classical metallic bolometer developed by Langley as early as 1878. However, the implementation of thermal decoupling from the substrate and the use of tunnel junctions for signal readout and reduction of electronic thermal conductivity allow these devices to achieve a sensitivity level comparable to that of cryogenically cooled Schottky diodes (see Table 1), while maintaining operability over a wide temperature range.

For moderate bias voltages, the theoretical current responsivity of a classical bolometer can reach $S_I = dI/dP = 1/V$ as the bias decreases down to $V = kT/e$, which corresponds to the ultimate bolometric responsivity $S_I = dI/dP = e/kT$. Multiplying by the resistance of the structure yields the voltage responsivity $S_V = dV/dP = eR/kT$. By increasing the normal-state resistance of the tunnel junctions, it is theoretically possible to achieve a high voltage responsivity in MIMIM detectors operating in the quantum response regime with multiplication of the number of excited electrons (Devyatov et al., 2006). In the case of quantum absorption without sufficient thermalization, the responsivity may decrease and approach that of a photon counter, where the current responsivity is limited to one electron per photon: $S_I = e/hf = 900$, while for thermalized carriers, it can reach $S_I = e/kT = 4 \times 10^4$ (for 300 GHz and 0.3 K).

The estimated ultimate performance parameters of MIMIM quantum detectors at 0.28, 4.2, 77, and 300 K are presented in Table 3.

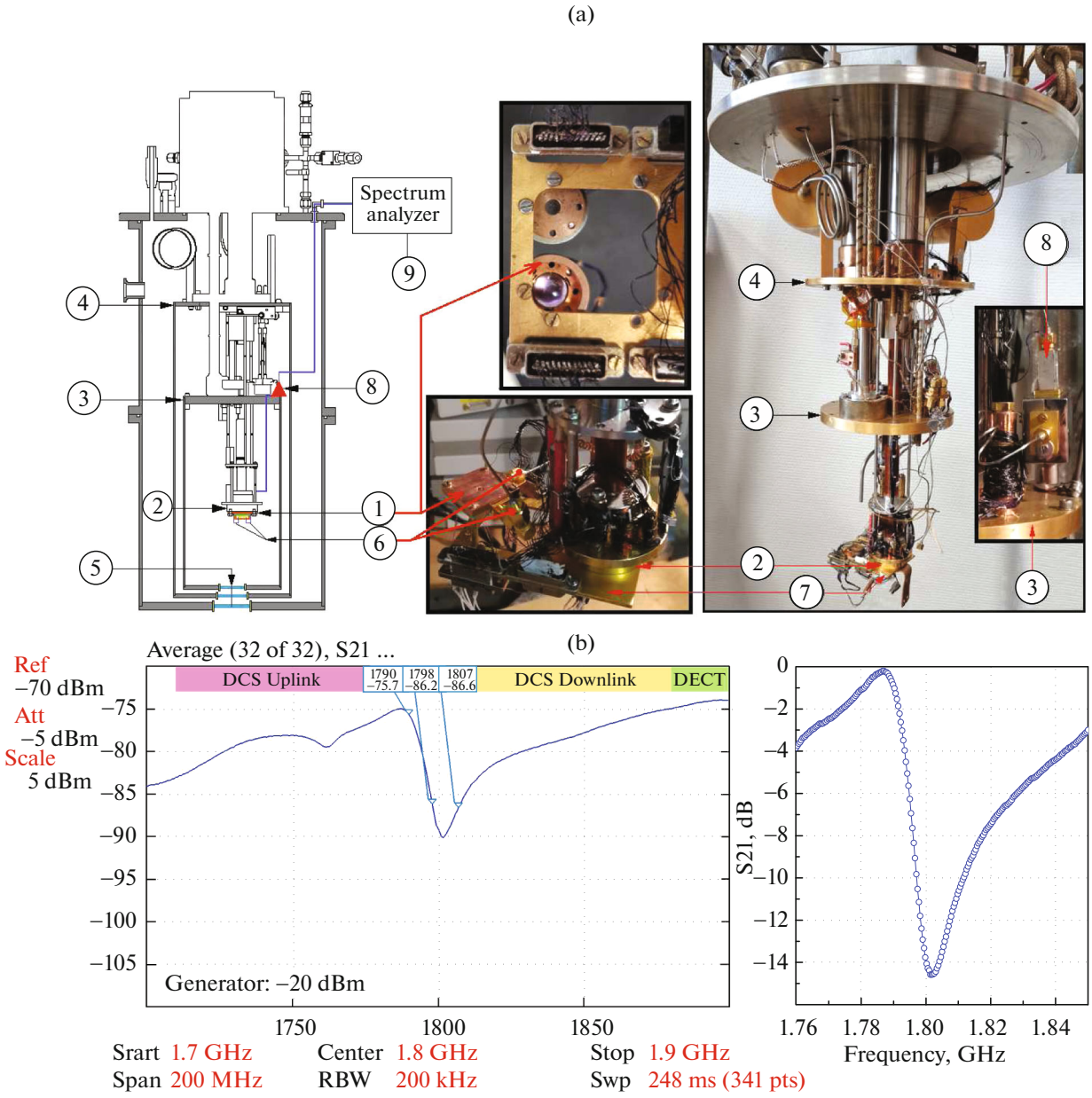

Fig. 7. Experimental setup (a) and results of SINIS detector studies using the microwave readout system (b). Panel (a): 1—the test sample mounted in a custom holder; 2—cold plate of the cryostat (minimum achievable temperature 276 mK); 3—second stage of the cryocooler (PTC 2nd stage, temperature: 2 K); 4—first stage of the cryocooler (PTC 1st stage, temperature: 55 K); 5—shield windows in the cryostat; 6—coaxial line for measurements with coplanar resonators; 7—mounting bracket attached to the cryostat cold plate for positioning the test samples; 8—HEMT amplifier (noise temperature: 5 K; lower-noise options are available, e.g., from Low Noise Factory (https://lownoisefactory.com/product-category/cryogenic-amplifier/)), installed on the 2 K stage; 9—spectrum analyzer. Panel (b): measured resonance response (without external irradiation) of the SINIS structure with an integrated coplanar resonator, designed for a 2 GHz resonance frequency at an operating temperature of 0.3 K.

8. PIXEL DESIGN FOR A 90 GHz BAND DETECTOR

The detector array based on planar ring antennas integrated with SINIS detectors (see Fig. 9a) consists of a series connection of 36 planar ring antennas. To enable proper electrical contact with the matrix, the chip includes four contact pads, allowing for a four-probe measurement configuration. This approach helps eliminate the influence of parasitic resistance introduced by the connecting wires.

The spectral response of this structure (Balega et al., 2024; Fig. 9b) was measured using a three-reference-channel technique to obtain a "cleaner" amplitude-frequency characteristic. A detailed de-

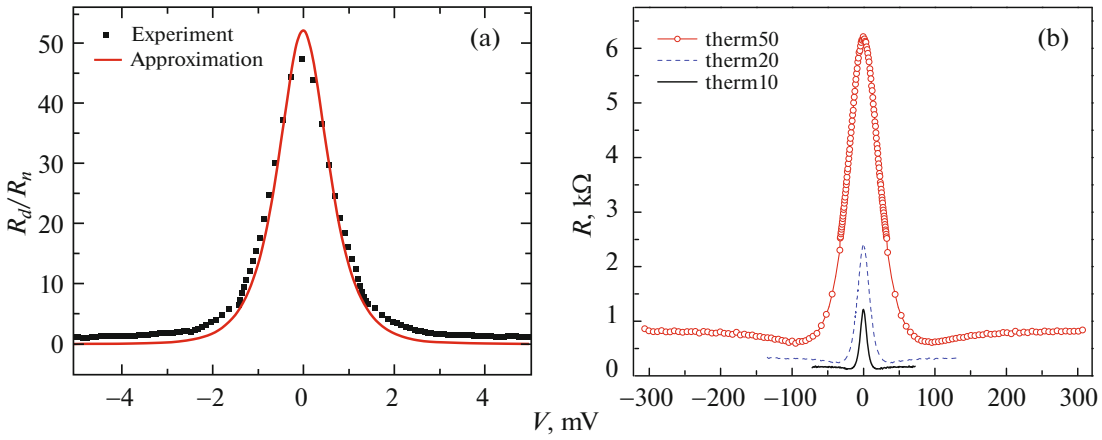

Fig. 8. Differential resistance of two SIN junctions (a) and chains of 10, 20, and 50 SIN junctions (b).

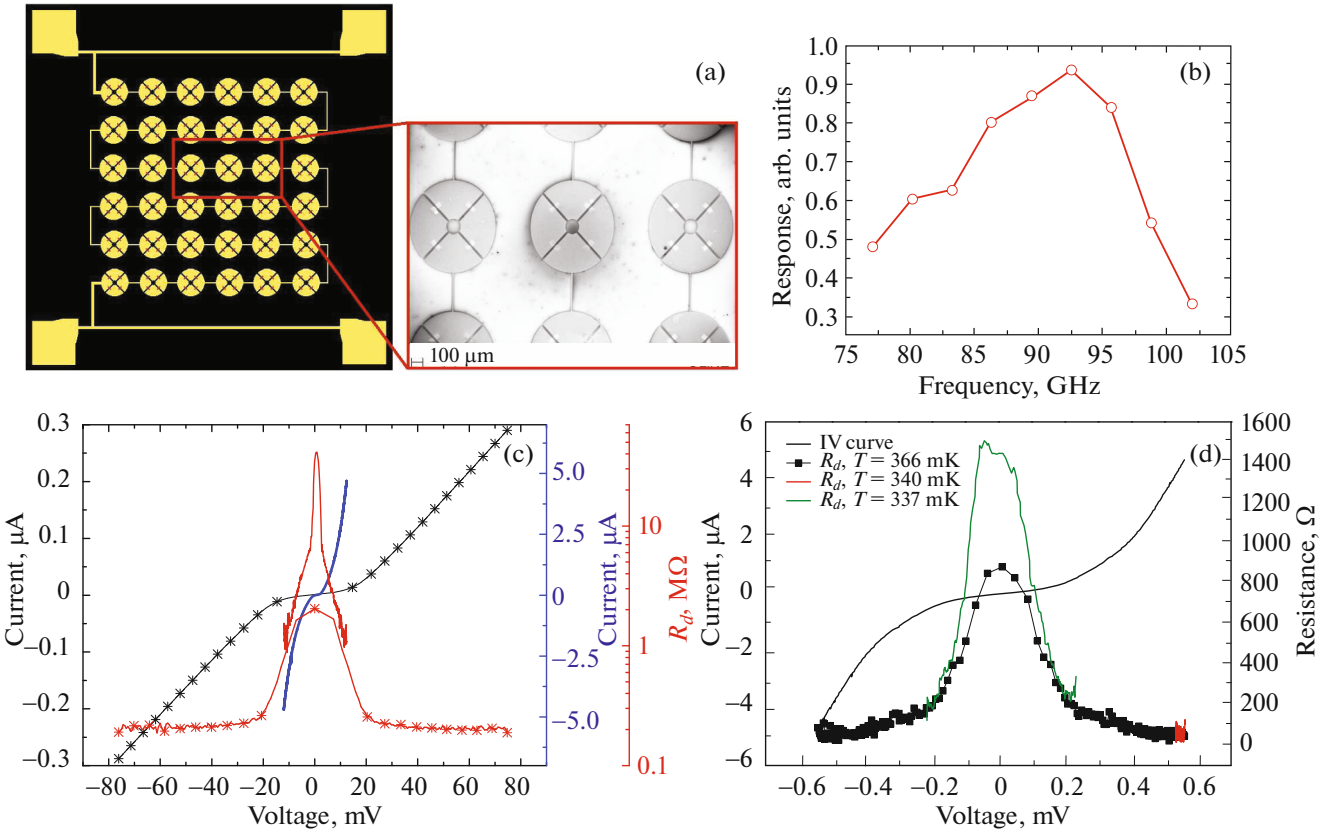

Fig. 9. 90 GHz detector array: layout and scanning electron microscope image of a matrix fragment (a); measured spectral response of the array (b); measured current-voltage characteristics (IV curves) and dynamic resistance R_d for a matrix with series-connected elements (Tarasov et al., 2024) (c); measured IV curves and R_d at different temperatures for a matrix with parallel-connected elements (d).

scription of the measurement methodology for such receiver arrays is provided in Gunbina et al. (2020). Numerical modeling results of the structure for both illumination from the substrate side and from the antenna side are also presented in Balega et al. (2024).

Additionally, we fabricated a similar matrix with a parallel connection of elements (low-impedance design). The measured current-voltage characteristics (IV curves) and dynamic resistance R_d at various temperatures for this structure are shown in Fig. 9d.

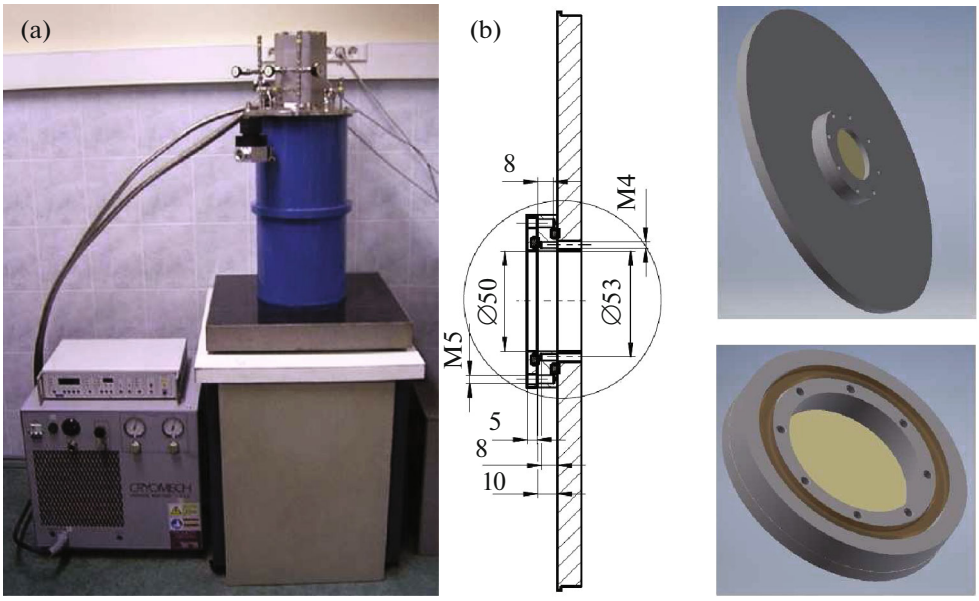

Fig. 10. Cryogenic system: photograph of the cryogenic setup (a); schematic drawing and 3D model of the optical window assembly (b). Dimensions are given in millimeters. M4 and M5 indicate the respective metric thread sizes of fastening elements.

9. CRYOGENIC SYSTEM

The primary concept of the cryogenic system is based on a closed-cycle cryostat utilizing a helium pulse-tube cooler, capable of reaching temperatures in the range of 2.5–4 K. To achieve further cooling to the sub-kelvin level required for SINIS detectors, the system incorporates a Helium-3 sorption cooler insert (Heliox AC-V, Oxford Instruments; see Fig. 10a). The standard laboratory Heliox cryostat has been modified for astronomical use on the telescope. In particular, a quasi-optical vacuum window has been designed and installed in the bottom flange of the cryostat (Fig. 10b). A blind-threaded mounting design was selected to secure the window. The system also allows for replacement of the optical windows, including additional filtered windows mounted on two radiation shields located at intermediate temperature stages of 100 K and 2.8 K. At present, the cryogenic system has been fully equipped with the necessary mechanical and electrical interfaces and is ready for installation in the Nasmyth focus cabin of the 6-m BTA telescope.

Alongside the primary cryogenic system, several alternative configurations were considered. One such option also employs a closed-cycle mechanical cryocooler (MCC) based on a pulse-tube refrigerator for precooling and includes a helium recondenser system as described earlier (Section 6) (Edelman and Yakopov, 2013), along with a liquefaction loop. This arrangement enables prolonged maintenance of operational temperatures even with the MCC compressor turned off.

A backup cryogenic system without MCC was also developed. This design features no moving mechanical components but requires periodic refilling with cryogens—specifically, liquid helium (Edelman, 2009).

Both alternative systems have been tested and are fully operational (see references), although they still require integration of an optical window for telescope operation.

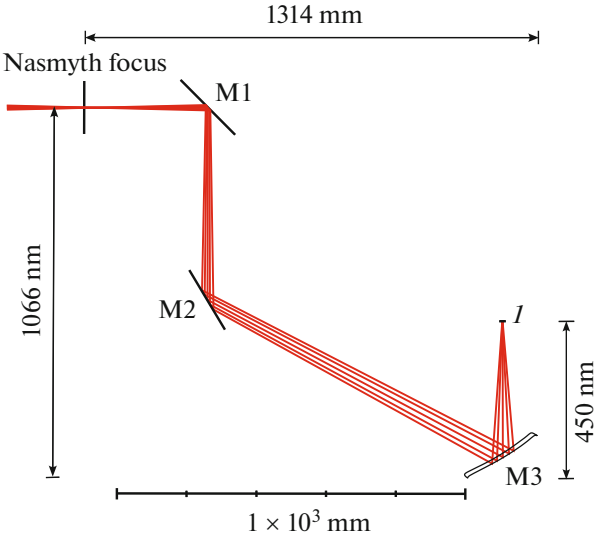

Fig. 11. Optical layout of the matching optics: two flat mirrors, $M1$ and $M2$, and an off-axis paraboloid, $M3$.

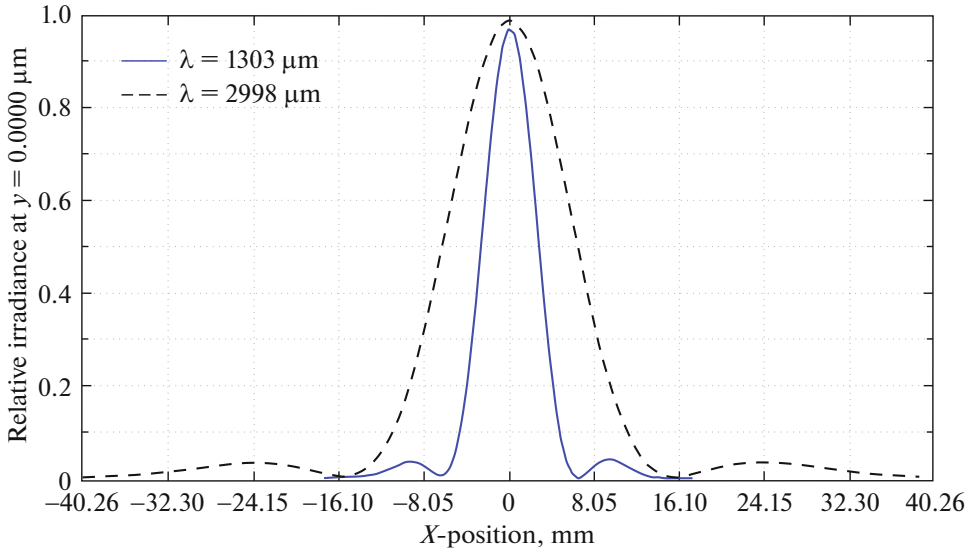

Fig. 12. Dimensions of the diffraction-limited spot at the horn aperture for wavelengths $\lambda = 1303$ μm (230 GHz) and $\lambda = 2998$ μm (100 GHz).

10. CORRECTIVE OPTICS

An optical and mechanical interface system was developed to integrate the sub-THz receiver into the Nasmyth focus of the BTA optical telescope. A key component of this interface is the corrective optical assembly. Initially, a scheme with a single inclined flat mirror for field scanning was considered. However, due to design constraints, this mirror would have required a diameter of 700 mm.

To reduce the size, an alternative configuration was implemented using two smaller flat mirrors (Fig. 11). In this design, light from the telescope's secondary mirror is first reflected off the flat mirror ($M1$), positioned at a 45° angle to the optical axis (mirror diameter 200 mm), then onto the second flat mirror ($M2$), tilted at 59° (also 200 mm in diameter), and finally directed onto an off-axis parabolic mirror $M3$ (diameter 200 mm). The image plane of $M3$ is aligned with the cryostat's input window. The off-axis paraboloid has a radius $r = 500$ mm and a focal length $f' = 250$ mm. The resulting relative aperture at the image plane is 1:8.3, corresponding to a numerical aperture of 0.12.

This optical system yields a beam divergence of approximately 13°.8. The diameter of the diffraction-limited spot is approximately 13 mm at a wavelength of 1303 μm (0.23 THz) and 30 mm at 2998 μm (0.1 THz), as shown in Fig. 12. Image scanning will be performed exclusively at the Nasmyth focus, which requires moving only a single mirror ($M2$, Fig. 11). With a mass of approximately 1 kg, this mirror can be tilted using a mechanical pusher with an eccentric mechanism. This approach was chosen over the initially considered piezoelectric actuator.

To enable field scanning, a mechanism for the synchronous oscillation of flat mirrors can be developed using mechanical pushers based on a cam mechanism. Given the compact dimensions of the optical elements, this approach does not pose significant technical difficulties. This scanning method is considered as a potential solution for future development. Its implementation is not technically demanding, and the authors have prior experience in constructing similar systems.

The proposed optical layout offers several advantages, including the reduced size of its components and the possibility of integrating an auxiliary optical sighting channel (via an additional foldable flat mirror and a lens-based compensator located after the parabolic mirror). The main disadvantages include additional reflection from the flat mirror, which leads to transmission losses, as well as relatively large diameters of the diffraction-limited spot.

Oscillation of mirror $M2$ provides beam modulation—i.e., angular deflection of the "receiver input" by at least one beamwidth relative to the observed object. In this configuration, the input alternates between the antenna and a reference position—typically a nearby patch of sky. Signal extraction is performed using a digital synchronous detection method, with a modulation reference signal synchronized to the pusher control unit, implemented via the standard plugin module in the IRTECON software package.

The modulation frequency can be set relatively high, within the range of 250—350 Hz. This effectively suppresses power line interference at 50 Hz as well as numerous harmonic components from the

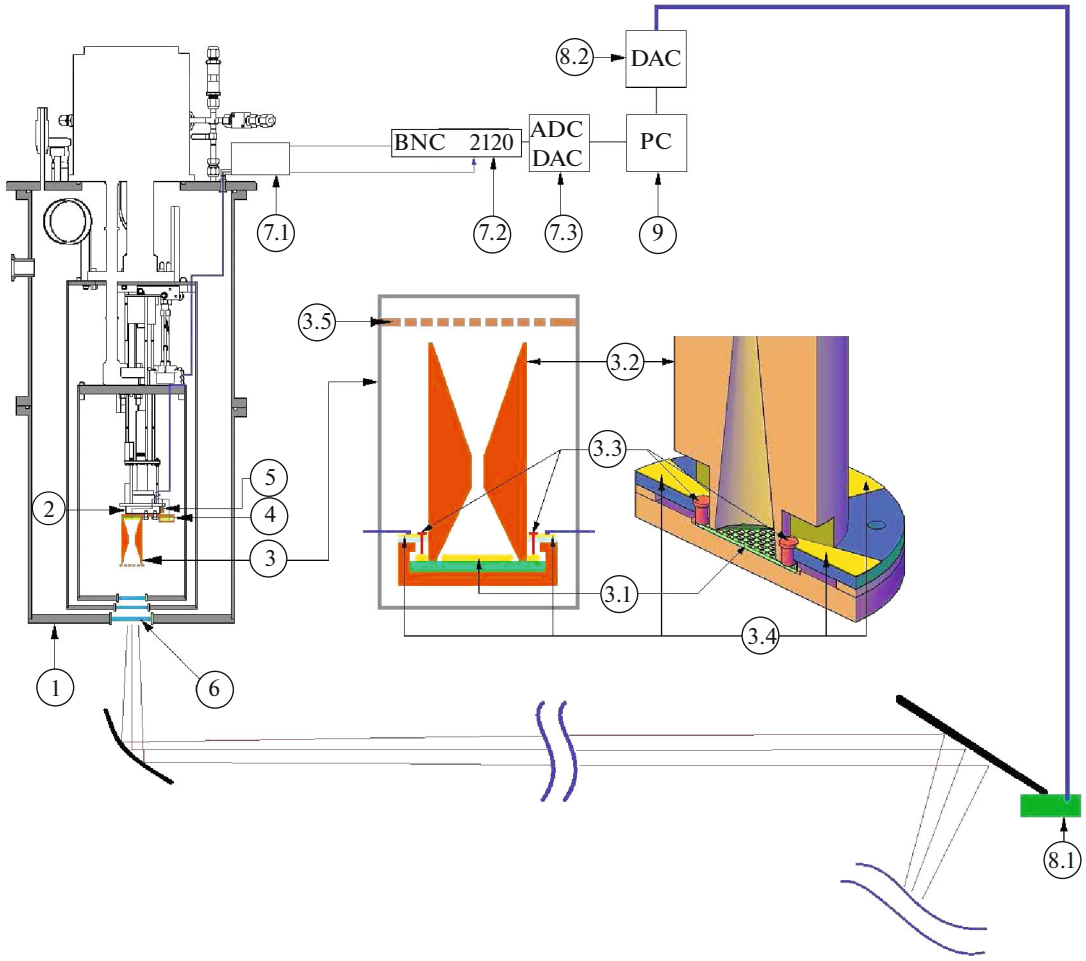

Fig. 13. General view of the observation system: 1—cryostat; 2—cold stage of the cryostat (operating temperature: 0.3 K); 3—detector assembly: 3.1—receiver array with integrated SINIS detectors; 3.2—part of the sample holder with back-to-back horn structure; 3.3—pogo-pin contacts for electrical connection to the contact pads of the receiver array; 3.4—contact pads on the fiberglass adapter plate into which the pogo-pins are soldered; 3.5—optical filter; 4—"dark" (reference) sample: an identical receiver array enclosed in a fully sealed copper holder; 5—thermometer on the cryostat cold stage; 6—vacuum windows with filters on the cryostat base for coupling incoming radiation to the receiver array; 7—readout/control electronics: 7.1—readout unit based on instrumentation amplifiers; 7.2—BNC-2120 switching board; 7.3—National Instruments analog-to-digital and digital-to-analog converters; 8—beam modulation system: 8.1—shear piezo actuator for mirror tilt control; 8.2—DAC for actuator control; 9—control computer with specialized software (`IRTECON`) for signal acquisition from the detector unit and piezo actuator control.

pulse tube valve switching unit, which typically appear in the 1–30 Hz range.

11. GENERAL VIEW OF THE SUB-THz OBSERVATION SYSTEM ON THE BTA TELESCOPE

A general schematic of the sub-terahertz observation system implemented on the BTA telescope is shown in Fig. 13. The incoming signal, collected by the primary telescope mirror, is directed toward the cryostat window. The optical path includes a set of specialized quasi-optical components designed to shape the incoming beam and guide it into the cryostat window (details are described in Section 10).

Inside the cryostat, a detector unit is mounted on the cold stage (operating at 0.28–0.3 K) using a dedicated sample holder with a back-to-back horn configuration, ensuring optimal coupling between the incident signal and the detector matrix.

In addition to the main detector matrix, a "dark" (reference) sample is also installed on the cold stage. This reference matrix is structurally identical to the main detecting matrix but is fully shielded from external radiation by an opaque enclosure. A similar approach was employed in laboratory experiments described by Gunbina et al. (2020), where a ruthenium resistor placed near the sample served as a reference

channel. In the current implementation, the dark matrix replaces the resistor.

Both the main and dark detector arrays are fabricated using a unified technological process on a single substrate, ensuring minimal variation in parameters. This eliminates systematic errors and ensures accurate comparative measurements.

Electrical contact with the detector matrix is made via spring-loaded pogo-pin connectors, precisely aligned with the matrix's contact pads through dedicated apertures in the sample holder. These pogo-pins are soldered into a fiberglass spacer fixed to the holder. As demonstrated by repeated thermal cycling, this configuration remains robust, enabling multiple reuses of the same sample holder without degradation-consistent with the durability observed in Tarasov et al. (2020b). The signal leads exit the cryostat through a vacuum feedthrough and terminate at an external connector, interfacing with the readout electronics. In the case of ground-based observations using a single-pixel configuration, a "conventional" readout circuit based on JFET transistors will be employed. This approach has been extensively validated for SINIS-detectors and remains the standard in low-noise cryogenic applications. The detailed schematic and performance characteristics of this readout system are provided in Section 5.1. Beam modulation (detailed in Section 11) is achieved by oscillating the secondary mirror with a piezoelectric shift actuator. Control of the piezo actuator and data acquisition are carried out using the IRTECON software suite, as illustrated in previous projects by Ermakov et al. (2001). This integration of modular hardware and software enables precise synchronous detection via beam chopping, while maintaining simplicity in system architecture.

12. CONCLUSIONS

This work presents a comprehensive overview of the development and integration of a sub-THz radiometer based on SINIS detectors into the instrumental complex of the BTA optical telescope. A batch of antenna matrices operating at 90 GHz with SINIS detectors optimized for cryogenic temperatures in the range of 100–300 mK, NEP = 10^{-17} W Hz$^{-1/2}$ was fabricated and successfully tested under laboratory conditions.

To achieve optimal responsivity across a broad temperature range, SINIS structures with suspended absorbers above the substrate were designed and manufactured. We investigated SINIS detectors based on Al–AlO_x–Nb tunnel junctions for operation at 2–8 K with an expected optical NEP = 10^{-14} W Hz$^{-1/2}$. In addition, metal–dielectric–metal–dielectric–metal (MDMDM) structures were studied, which are suitable for operation up to room temperature and are predicted to achieve NEP = 10^{-12} W Hz$^{-1/2}$. A range of planar quasi-optical bandpass filters, including those centered at 90 GHz, and high-efficiency bulk high-pass filters were developed and fabricated (Tarasov et al., 2024). As a result, the first domestic prototype of a superconducting sub-THz receiver intended for integration into an astronomical observatory has been developed.

This system includes a full set of required components and auxiliary subsystems necessary for astronomical observations: proven readout electronics, cryogenic vacuum systems for deep cooling of superconducting detectors, and an optical system complete with mechanical, optical, and cryogenic interfaces.

ACKNOWLEDGMENTS

The authors express their gratitude to the institutions operating the unique scientific infrastructure facilities: UNU "Kriointegral" (No. 352529), UNU "CKP-7" (No. 3589084) and UNU "BTA" (No. 73609), for providing access to the equipment used in this study. The fabrication of SINIS detector sample structures was carried out using the equipment at UNU "Kriointegral". The development and production of various electrical and mechanical interfaces required for detector characterization, as well as work related to cryo-vacuum system integration, were performed at UNU "CKP-7". The optical layout design and the preparation of the test observation platform were conducted using the scientific infrastructure of UNU "BTA".

FUNDING

The research on the core system concept including SINIS detectors, readout electronics, cryostat system, and corrective optics was supported by the Russian Science Foundation (grant no. 23-62-10013 (https://rscf.ru/project/23-62-10013/)).

The development of Nb–AlO_x–Al structures and MDMMDM-type detectors was funded by the Ministry of Science and Higher Education of the Russian Federation under project No. 075-15-2024-482.

CONFLICT OF INTEREST

The authors of this work declare that they have no conflicts of interest.

REFERENCES

1. S. Ariyoshi, T. Taino, A. Dobroiu, et al., Applied Physics Letters **95** (19), id. 193504 (2009). https://doi.org/10.1063/1.3263711
2. S. Ariyoshi, K. Takahashi, T. Noguchi, et al., Superconductor Science and Technology **25** (7), article id. 075011 (2012). https://doi.org/10.1088/0953-2048/25/7/075011
3. J. W. M. Baars, *The Paraboloidal Reflector Antenna in Radio Astronomy and Communication* (Springer, Berlin, 2007). https://doi.org/10.1007/978-0-387-69734-5
4. Y. Balega, G. Bubnov, A. Chekushkin, et al., Sensors **24** (2), id. 359 (2024). https://doi.org/10.3390/s24020359
5. J. Bueno, V. Murugesan, K. Karatsu, et al., Journal of Low Temperature Physics **193**, 96 (2018). https://doi.org/10.1007/s10909-018-1962-8
6. Y. Chai, S. Shu, Y. Li, et al., Journal of Low Temperature Physics **214** (3), 210 (2024). https://doi.org/10.1007/s10909-023-03040-7
7. I. A. Devyatov, P. A. Krutitskiĭ, and M. Yu. Kupriyanov, JETP Letters **84**, 57 (2006). https://doi.org/10.1134/S0021364006140037
8. J. Du, K. Smart, L. Li, et al., Superconductor Science and Technology **28** (8), article id. 084001 (2015). https://doi.org/10.1088/0953-2048/28/8/084001
9. V. Edelman, Instruments and Experimental Techniques **52**, 301 (2009). https://doi.org/10.1134/S002044120902033X
10. V. Edelman and G. Yakopov, Instruments and Experimental Techniques **56**, 613 (2013). https://doi.org/10.1134/S002044121305014X
11. A. B. Ermakov, S. V. Shitov, A. M. Baryshev, et al., IEEE Transactions on Applied Superconductivity **11** (1), 840 (2001). https://doi.org/10.1109/77.919475
12. A. Generalov, J. Holstein, A. Murros, et al., ACS Applied Electronic Materials **6** (4), 2197 (2024). https://doi.org/10.1021/acsaelm.3c01511
13. M. J. E. Golay, Review of Scientific Instruments **18** (5), 347 (1947). https://doi.org/10.1063/1.1740948
14. A. Gunbina, S. Mahashabde, M. Tarasov, et al., IEEE Transactions on Applied Superconductivity **31** (5), id. 3068999 (2021a). https://doi.org/10.1109/TASC.2021.3068999
15. A. Gunbina, M. Tarasov, M. Fominsky, et al., "*Fabrication of Aluminium Nanostructures for Microwave Detectors Based on Tunnel Junctions*" in *Advances in Microelectronics Reviews, Vol. 3*, Ed. by S. Y. Yurish (IFSA Publishing, Barcelona, Spain) **3**, 183–211 (2021b).
16. A. A. Gunbina, M. A. Tarasov, S. A. Lemzyakov, et al., Physics of the Solid State **62**, 1604 (2020). https://doi.org/10.1134/S1063783420090097
17. J. Henning, P. Ade, K. Aird, et al., SPIE Conf. Proc. **8452**, article id. 84523A (SPIE, 2012). https://doi.org/10.1117/12.927172
18. B. S. Karasik and R. Cantor, Applied Physics Letters **98** (19), id. 193503 (2011). https://doi.org/10.1063/1.3589367
19. M. A. Markina, A. M. Chekushkin, M. A. Tarasov, et al. Technical Physics **69** (7), 1004 (2024). https://doi.org/10.61011/JTF.2024.07.58343.169-24
20. A. V. Merenkov, T. M. Kim, V. I. Chichkov et al. **64** (10), 1387 (2022). https://doi.org/10.21883/FTT.2022.10.53081.50HH
21. O. V. Minin, J. Calvo-Gallego, Y. M. Meziani, and I. V. Minin, Applied Sciences **11** (15), id. 7011 (2021). https://doi.org/10.3390/app11157011
22. R. Müller, B. Gutschwager, J. Hollandt, et al., Journal of Infrared, Millimeter, and Terahertz Waves **36**, 654 (2015). https://doi.org/10.1007/s10762-015-0163-7
23. C. Nunez, J. W. Appel, S. M. Bruno, et al., SPIE Conf. Proc. **12190**, id. 121901J (2022). https://doi.org/10.1117/12.2630081
24. A. G. Paulish, A. V. Gusachenko, A. O. Morozov, et al., Sensor Review **40** (3), 291 (2020). https://doi.org/10.1108/SR-03-2020-0047
25. A. Prikhodko, I. Belikov, D. Mikhailov, et al., Journal of Physics: Conf. Ser. **2086**, id. 012063 (2021). https://doi.org/10.1088/1742-6596/2086/1/012063
26. A. Rogalski, Journal of Infrared, Millimeter, and Terahertz Waves **43** (9), 709 (2022). https://doi.org/10.1007/s10762-022-00882-2
27. J. Sayre, P. Ade, K. Aird, et al., SPIE Conf. Proc. **8452**, article id. 845239 (2012). https://doi.org/10.1117/12.927035
28. D. Schmidt, K. Lehnert, A. Clark, et al., Applied Physics Letters **86** (5), id. 053505 (2005). https://doi.org/10.1063/1.1855411
29. V. Stolyarov, Y. Balega, M. Mingaliev, et al., Astrophysical Bulletin **79** (2), 321 (2024). https://doi.org/10.1134/S1990341324600467
30. M. Tarasov, A. Gunbina, A. Chekushkin, et al., Applied Sciences **12** (20), id. 10525 (2022). https://doi.org/10.3390/app122010525
31. M. Tarasov, A. Gunbina, A. Krasilnikov, et al., in *2024 IEEE 9th All-Russian Microwave Conference (RMC), Moscow, Russian Federation, 2024* (IEEE, 2024), pp. 176–179. https://doi.org/10.1109/RMC62880.2024.10845907
32. M. Tarasov, A. Gunbina, M. Fominskii, and A. Chekushkin, Application for a Russian patent for an invention RU **2757762** (2021a). [in Russian]
33. M. Tarasov, Yu. Nagirnaya, Yu. Gunbina, et al., Application for a Russian patent for an invention RU **2749575** (2021b). [in Russian]
34. M. A. Tarasov, V. S. Edelman, S. A. Lemzyakov, et al., in *2020 7th All-Russian Microwave Conference (RMC), Moscow, Russian Federation, 2020*, (IEEE, 2020a), pp. 25–27. https://doi.org/DOI:10.1109/RMC50626.2020.9312267

35. M. A. Tarasov, S. Mahashabde, A. A. Gunbina, et al., Physics of the Solid State **62**, 1580 (2020b). https://doi.org/10.1134/S1063783420090292
36. A. Vystavkin, S. Shitov, S. Bankov, et al., Radiophysics and Quantum Electronics **50**, 852 (2007).
37. R. Yadav, F. Ludwig, F. R. Faridi, et al., Sensors **23** (7), 3469 (2023). https://doi.org/10.3390/s23073469
38. G. Yakopov, M. Tarasov, A. Gunbina, et al., in *EPJ Web of Conferences*, vol. 195, id. 05014 (EDP Sciences, 2018). https://doi.org/10.1051/epjconf/201819505014
39. S. Yates, J. Baselmans, A. Endo, et al., Applied Physics Letters **99** (7) id. 073505 (2011). https://doi.org/10.1063/1.3624846
40. R. Zhou and J. T. Yeow, IEEE Nanotechnology Magazine (online https://inm.ieeenano.org/2024-october-issue-nanotechnology-progress-results/) (2024). https://doi.org/10.1109/MNANO.2024.3436328

Translated by E. Porfiryeva